APPLIED PHYSICS

Membrane insertion of—and membrane potential sensing by—semiconductor voltage nanosensors: Feasibility demonstration

Kyoungwon Park,[1] Yung Kuo,[1] Volodymyr Shvadchak,[2] Antonino Ingargiola,[1] Xinghong Dai,[3] Lawrence Hsiung,[4] Wookyeom Kim,[5] Hong Zhou,[3,6] Peng Zou,[7]* Alex J. Levine,[1,8] Jack Li,[1] Shimon Weiss[1,6,9]†

We developed membrane voltage nanosensors that are based on inorganic semiconductor nanoparticles. We provide here a feasibility study for their utilization. We use a rationally designed peptide to functionalize the nanosensors, imparting them with the ability to self-insert into a lipid membrane with a desired orientation. Once inserted, these nanosensors could sense membrane potential via the quantum confined Stark effect, with a single-particle sensitivity. With further improvements, these nanosensors could potentially be used for simultaneous recording of action potentials from multiple neurons in a large field of view over a long duration and for recording electrical signals on the nanoscale, such as across one synapse.

INTRODUCTION

Recent advances in inorganic colloidal synthesis methods have afforded the construction of functional semiconductor (SC) nanoparticles (NPs) with ever-increasing control over size, shape, composition, and sophisticated heterostructures that exhibit unique photophysical, chemical, and electronic properties (1–4). This precise command of nanoscale materials synthesis has allowed for the exquisite engineering of excited-state wavefunctions (5–7), charge confinement, spatiotemporal control of charge-separated states (8), and manipulation of Fermi levels and redox potentials. As a result, SC NPs have proved to be very useful in numerous applications in optoelectronics (9, 10), biological imaging (11), sensing (12–14), catalysis (15), and energy harvesting (16).

Integrating inorganic nanomaterials with naturally evolved or synthetically evolved biological machineries could, in principle, yield highly sophisticated hybrid nanobiomaterials that outperform biological-only or inorganic-only materials (17). These materials could be self-assembled by biomolecular recognition while maintaining the superior properties of inorganic materials (18, 19). Self-assembly of inorganic components by biomolecular recognition could align components in defined geometries, spatial orientations, and structures. In addition, careful design and control of the organic-inorganic interface could afford hybridization of electronic states, enhancement of radiationless energy transfer or electron transfer, or matching of Fermi levels with redox potentials.

Numerous functionalization and bioconjugation methods have been developed for the integration of inorganic-biological hybrid nanomaterials that are water-soluble and biologically active (20, 21). These hybrid nanomaterials have been used for in vitro biosensing, intracellular biological imaging (22), single-protein tracking in live cells (20), and in vivo molecular imaging with favorable in vivo biodistribution and targeting properties (including renal clearance) (11, 23, 24).

Much fewer attempts have been made to functionalize nanomaterials in a way that will allow their integration into the membrane. The ability to impart membrane protein–like properties to NPs could afford their targeting and insertion into the lipid bilayer and the construction of membrane-embedded hybrid nanomaterials with useful functions. For example, a few attempts have been made to target and insert (very small, <3 nm) SC quantum dots (QDs) into the lipid bilayer. Al-Jamal et al. (25) incorporated very small QDs in between the two lipid layers of the vesicle's bilayer, as proven by fluorescence microscopy. Kloepfer et al. (26) reported the transmission electron microscopy (TEM) micrographic evidence of QDs inserted into vesicles' membranes. Gopalakrishnan et al. (27) successfully delivered lipophilic QDs (that were first loaded to vesicles' membranes) into membranes of human embryonic kidney (HEK) 293 cells via vesicle fusion. Wi et al. (28) investigated the maximum allowed QDs' size both experimentally and theoretically that could still afford membrane insertion. Recently, insertion of other types of nanomaterials into the membrane was demonstrated. Synthetic ion channels made from DNA nanostructures (29, 30) and ion channels made from carbon nanotubes (31) were successfully inserted into lipid bilayers while maintaining functional ion transport across the membrane.

Following works on asymmetric type-II (conduction band and valence band minima are spatially separated) seeded nanorods (NRs) at low temperature on the single-particle level (6, 32) and at room temperature on the ensemble level (33), we recently demonstrated that these NRs exhibit a large quantum-confined Stark effect (QCSE) at room temperature on the single-particle level (34). Marshall and Schnitzer (35) calculated the QCSE of simple type-I QDs (conduction band and valence band minima spatially overlapped) and showed that they have high enough sensitivity to detect action potential with superior signal-to-noise (S/N) ratio to the conventional voltage sensitive dyes. Although recently developed voltage indicators provide much improved sensitivity (36, 37), QCSE of asymmetric type-II NRs is predicated to exhibit

[1]Department of Chemistry and Biochemistry, University of California, Los Angeles, Los Angeles, CA 90095, USA. [2]Institute of Organic Chemistry and Biochemistry AS CR, Prague 166-10, Czech Republic. [3]Department of Microbiology, Immunology, and Molecular Genetics, University of California, Los Angeles, Los Angeles, CA 90095, USA. [4]Department of Chemical and Biomolecular Engineering, University of California, Los Angeles, Los Angeles, CA 90095, USA. [5]Department of Ecology and Evolutionary Biology, University of California, Los Angeles, Los Angeles, CA 90095, USA. [6]California NanoSystems Institute, University of California, Los Angeles, Los Angeles, CA 90095, USA. [7]Department of Chemistry and Chemical Biology, Harvard University, MA 02138, USA. [8]Department of Physics, University of California, Los Angeles, Los Angeles, CA 90095, USA. [9]Department of Physiology, University of California, Los Angeles, Los Angeles, CA 90095, USA.
*Present address: College of Chemistry and Molecular Engineering, Peking University, China.
†Corresponding author. Email: sweiss@chem.ucla.edu

even higher voltage sensitivity (38). However, to the best of our knowledge, no attempts have been made to target and insert rod-shaped NPs into the lipid bilayer. In particular, membrane insertion of NRs with length larger than the membrane thickness (~4 nm) has not been demonstrated thus far. We present here an approach to insert and position NRs in the membrane by imparting them with membrane protein–like properties and report on membrane voltage–sensing experiments with these NPs.

RESULTS

NRs strongly change their emission in the electric field oriented along their long axis. The optimal strategy to use them for detection of transmembrane potential is to insert them perpendicularly to the membrane surface (Fig. 1A). Selective binding of cylindrical NRs to membranes in perpendicular orientation requires different lipophilic coating of the sides of the cylinder and hydrophilic coating of the tops. To make this nonhomogeneous coating, we decided to use different curvature of the surfaces. The tops of NRs that should bear more hydrophilic coating have higher curvature than cylinder sides. Our previously developed peptide-coating technique [developed for solubilizing QDs in hydrophilic environments (11, 39–43)] used flexible peptides that afforded uniform coating. For facet-selective coating, we designed a peptide consisting of hydrophobic rigid helical domain and more flexible hydrophilic domain (Fig. 1B). Preferential binding of rigid helical domain to the sides of the NR cylinder should lead to a significant difference in the lipophilicity of the sides and tops of the NR necessary for perpendicular insertion into membranes. The sequence of this prototype peptide is myristoyl-CLTCALTCMECTLKCWYKRGCRGCG-COOH, where the KRGCRGCG part served as the hydrophilic flexible segment, and other amino acids form an approximately 2.5-nm-long helix that is able to cover half of the NR cylinder side (Fig. 1). By simple geometrical considerations, we assess that ~8 to 12 peptides could self-assemble on a single NR (Fig. 1C) and cover it. Binding of the peptide to the NRs is
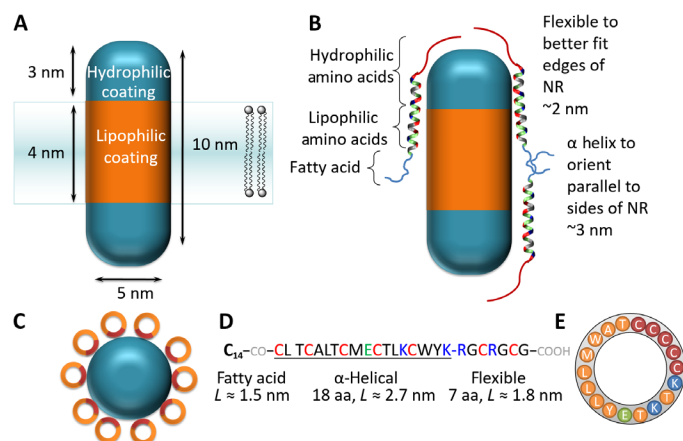
mediated by seven Cys residues: five on one face of the helical part and two in the flexible segment. To control the immersion depth of the peptide-covered NRs and to prevent insertion with a tilted orientation, we incorporated a KCWYK segment containing amino acids that preferentially localize at the membrane-water interface (44). Only a short segment of aliphatic amino acids was incorporated into the peptide sequence, including three hydroxyl-containing Thr residues and one acidic residue in the hydrophobic helical segment, to avoid aggregation in solution. More details regarding the peptide design are given in section S1. The α-helicity of the peptide was confirmed by circular dichroism spectroscopy (section S2 and fig. S1) in octanol solution (ε_r = 5.1 versus membrane ≈ 5).

To test the selective binding (perpendicular) of peptide-coated NRs (pcNRs) to membranes, we introduced them into small unilamellar vesicles (SUVs) and then imaged them by EM. Quasi type-II CdSe-seeded CdS rod [same recipe applied to the sample #3 of Park et al. (34)] with dimensions of 4 ± 0.3 nm in diameter and 10 ± 2.2 nm in length were used for this study. The wavelength's peak position (λ_{max}) and full width at half maximum are 604 nm and 30 nm, respectively. This seeded rod exhibits 4 nm of red shift at 400 kV/cm of the electric field in air (ε_r = 1). The asymmetric QCSE feature indicates the asymmetric localization of CdSe seed with respect to the center of the CdS rod (34). This rod is selected because the chemistry is well developed to yield narrow size distribution and its QCSE is confirmed at room temperature (34). The pcNRs containing SUVs were then flash-frozen and imaged by cryoEM (Fig. 2A and Materials and Methods). Because cryoEM images are two-dimensional projections, the exact z positions of pcNRs are not exactly known. For this reason, the level of insertion of pcNRs was assessed only for particles close to the vesicle's "equator." We analyzed more than 500 pcNRs and classified them into four categories (Fig. 2, B and C). The a-type represents an ideal, symmetric, and perpendicular insertion (the NR symmetrically traverses the membrane), which was observed for 16.4% of all analyzed pcNRs. The b-type represents partial (asymmetric) but perpendicular insertion (18% of all analyzed pcNRs). The c-type represents partial, tilted insertion and is the most abundant (41.7% of all analyzed pcNRs). The d-type represents horizontal insertion in between the two leaflets of the membrane (23.9% of all analyzed pcNRs). The histogram in Fig. 2C shows the partitioning in insertion geometries. If all cases of c-type insertion are ignored (because it is hard to classify parallel versus perpendicular insertion for these cases), then vertically oriented pcNRs (a- and b-type) constitute 59% of all a-type, b-type, and d-type insertions. Although these percentages are only a rough estimate for the partitioning between the different insertion configurations (because of the ambiguity in z positioning) and the captured cryoEM images only show frozen snapshots of NRs inserted into membranes, this estimate for partitioning is also reproduced in an independent fluorescence anisotropy measurement. The NRs were loaded into electro-swelled giant UVs (GUVs) (section S3). The orientation of the membrane-associated pcNRs was probed by polarization microscopy (45), capitalizing on the fact that the absorption and emission dipoles of NRs are aligned along their long axis (46). To estimate the orientation of pcNRs in the membrane, we imaged the fluorescence of GUVs loaded with pcNRs using linearly polarized laser excitation. Because the absorption and emission dipoles of NRs are aligned along their long axis, polarized excitation could verify the orientation of pcNRs with respect to the cellular membrane curvature (fig. S2). By analyzing the polarization anisotropy of individual pcNRs and applying a simple absorption anisotropy (AA) threshold, we could estimate that ~58% of the pcNRs were inserted with
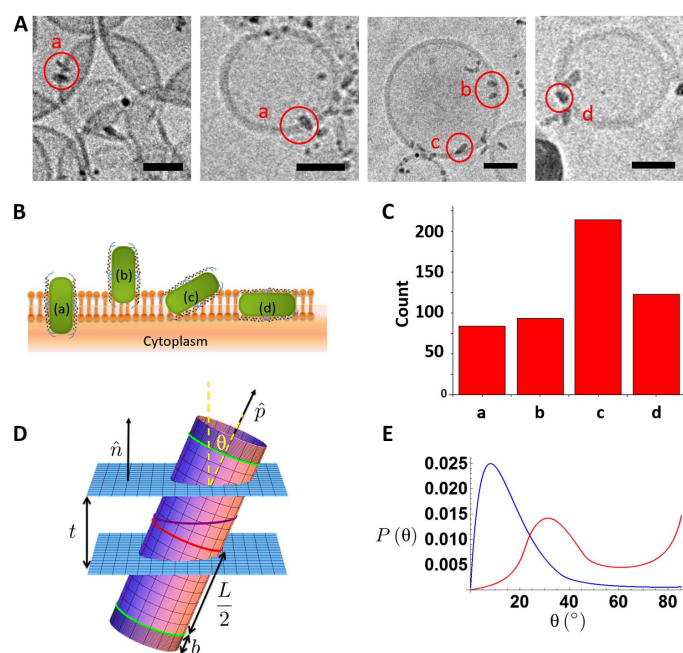

Fig. 1. Surface functionalization. (**A**) Cartoon describing design principles for rendering NR membrane protein–like properties. This functionalization will favor their stable, spontaneous insertion into the membrane with the correct orientation. (**B**) Peptide design for implementing (A). (**C**) Top view of an NR coated with peptides. Brown and orange colors depict Cys-rich and lipophilic faces of the α-helical peptide, respectively. (**D**) Sequence of the designed peptide. C_{14}-CO- stands for myristoyl acid residue attached to the N-terminal amino group. (**E**) Wheel diagram corresponding to the α-helical part of the peptide. Color coding is the same as in (C). aa, amino acid.

Fig. 2. NR interaction with membrane. (**A**) CryoEM micrographs of pcNRs inserted into SUVs. Scale bars, 30 nm. (**B**) Schematics of possible pcNRs association with lipid bilayer: (a) properly inserted, (b) partially inserted, (c) attached in an angle, and (d) horizontally embedded. (**C**) Histogram of insertion geometries (a) to (d). (**D**) Schematic of the NR of hydrophobic length L with two hydrophilic ends of length b and radius a. The total length of the rod is then $L + 2b$. It is shown in a piece of membrane of thickness t. The green curves show the ends of the hydrophobic rod. The red curve denotes the center of the nanostructure, whereas the purple curve shows the intersection of the rod with the mid-plane of the membrane. (**E**) Model calculations (see section S7) of canting angles (θ) probability distribution for a membrane-inserted NR. Calculations for no hydrophobic mismatch ($L = t = 4$ nm, blue) and for significant hydrophobic mismatch ($L = 6$ nm, $t = 4$ nm; red) are shown. In both cases, the rods are terminated at both ends by hydrophilic cylinders with a length of 2 nm (details of the model are discussed in section S7).

an orientation that is more perpendicular (threshold, >0), than parallel, to the membrane plane (section S3). In contrast to cryoEM snapshots, AA spectroscopy on the single-particle level could follow NR reorientation dynamics in real time. Moreover, it could help disentangle the blinking dynamics from reorientation dynamics if both horizontally and vertically polarized photons are measured simultaneously. We note that, despite the fact that we have tested thus far only one rationally designed α-helical peptide sequence, a sizeable fraction of pcNRs showed vertical membrane orientation (~58%), and 16% of NRs were properly inserted, supporting the feasibility of this functionalization approach. A control cryoEM experiment showed that as-synthesized (native ligand–coated) NRs do not insert into vesicles' membranes (section S6).

Because the polarization anisotropy of pcNRs in the vesicle fluctuates, we expect that pcNRs in the membrane are not rigid. Considering a simple estimate based on the NR diffusing in a solvent with a viscosity of 1 kg/m·s (a thousand times the viscosity of water), we obtain a rotational diffusion constant on the order of 10 kHz. This would suggest that the azimuthal angle should be rotationally averaged out on the time scale of the measurement. The observation of slower rotational fluctuations might be due to coupling to translational motion or to fluctuation in the level of insertion (that is, the NR moves in and out of the membrane). To assess the cryoEM results, we studied the equilibrium partitioning

between the membrane and the solution of the NRs, as well as their orientational fluctuations within the membrane using the Boltzmann distribution and a simple model of the interaction energy of the NR with the membrane and solvent (see Fig. 2D and section S7 for details).

We found that, for reasonable hydrophobic/hydrophilic energies and typical NR geometries, NRs strongly partition to the membrane. Once embedded in the membrane, we predict that rods will be canted so that their long axis does not lie along the local normal to the membrane. The mean canting angle (θ) depends on the mismatch of the length of the hydrophobic region of the NR and the thickness of the membrane. Examining that figure, we estimate the fluctuations of the canting angle of rods with no hydrophobic mismatch (blue curve) to be in the range of 10° and thus comparable to the mean. Both the mean and the fluctuations are larger for cases of large hydrophobic mismatch (red). We expect larger fluctuations for significantly larger angles based on the large tail of the angle probability distribution. This model predicts that with hydrophobic surfaces covering a length of the pcNRs comparable to the membrane thickness, the fraction of rods inserted into the membrane approaches unity in thermal equilibrium. To stabilize the orientation of rods in the membrane to be close to the membrane's normal, it is advantageous to include hydrophilic ends on the pcNR tips. For reasonable lengths of these ends, they do not significantly change the partitioning of rods between the membrane and the solvent. Moreover, the model predicts a canting angle distribution (Fig. 2E) that resembles the histogram in Fig. 2C, suggesting some degree of hydrophobic mismatch (Fig. 2D). However, we note that the statistical nature of ligand exchange with the designed peptide does not necessarily impart precise hydrophobic surfaces and hydrophilic tips. In addition, we emphasize that the cryoEM visualization of NRs in the vesicular membrane is only a proof-of-concept demonstration and does not serve as a proof for correct insertion into cellular membranes. At this point, we cannot rule out possible differences in membrane insertion geometry and/or efficiency between vesicular and cellular membranes. Such a comparison will be the subject of a future work.

pcNRs can be delivered to the cellular membrane by either vesicle fusion (Fig. 3, A to C) or direct drop-casting method (Fig. 3, E and F). Fusogenic lipids are required for vesicle fusion process. Here, we used 1,2-stearoyl-3-trimethylammonium-propane (DOTAP) or 3β-[N-(N′,N′-dimethylaminoethane)-carbamoyl]cholesterol hydrochloride (DC-Chol) and a cone-shaped lipid, 1,2-dioleoyl-sn-glycero-3-phosphoethanolamine (DOPE) (27, 47, 48). Once vesicles were formed, pcNRs were loaded, and their instantaneous staining could be observed (Fig. 3A). When pcNR-loaded vesicles were added to HEK293 tissue culture, they could be delivered to the cell membrane via fusion. Bright-field image (Fig. 3B) and its corresponding fluorescence image (Fig. 3C) capture the moment of vesicle fusion. Z-stack images of the same cell are shown in fig. S3, indicating vesicle fusion and subsequent membrane staining. The pcNRs could also be added directly to the growth medium of a tissue culture, as demonstrated in Fig. 3 (E and F) for HEK293 cells. By diluting the concentration of pcNRs, sparse labeling could be achieved such that individual (or small aggregates of) pcNRs could be observed (Fig. 3F). We observed a loss in the diffraction-limited fluorescence emanating from membrane inserted pcNRs within ~1 hour after staining, most likely due to endocytosis (fig. S5).

Membrane voltage sensing with pcNRs was first tested using self-spiking HEK293 cells (49). This cell line exhibits self-oscillations (~3 to 4 Hz) in membrane potential once cells reach confluency (49). Figure 4 shows optical recordings of these self-spiking HEK293 cells
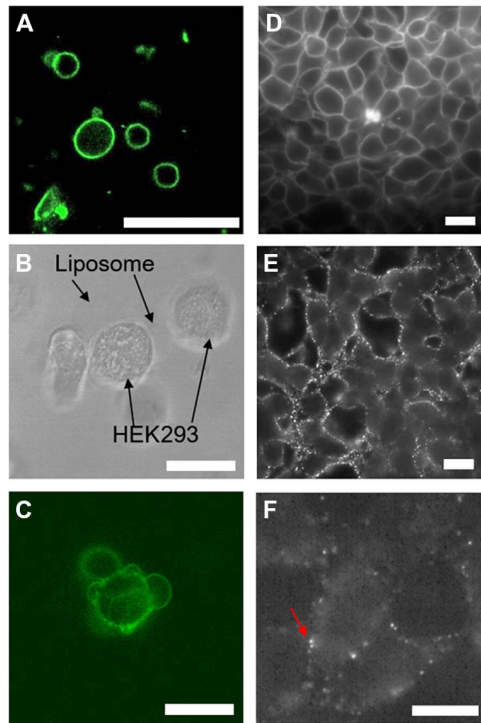
Fig. 3. Delivery of pcNRs to HEK293 cells. (**A**) Fluorescence of NR-loaded GUVs. (**B** and **C**) Bright-field (B) and fluorescence (C) images of pcNR-loaded GUV fused with the cell membrane. (**D**) Fluorescence image of HEK293 cells stained with ANEPPS (control). (**E** and **F**) pcNRs targeted to membranes at high (E) and low (F) concentrations. Scale bars, 10 μm.

with di-8-ANEPPS (ANEPPS) (Fig. 4, A, D, and E, serving as positive control) and pcNRs (Figs. 4, B, C, F, and G). Oscillating membrane potential is resolved by ANEPPS, exhibiting ~10% ΔF/F on the ensemble level (see Fig. 4D, top, and section S8 for image analysis details). Bottom of Fig. 4D shows four ΔF/F recordings (from four distinct locations, averaged over 5 × 5 pixels) marked with open circles of the same color. Figure 4A shows that these recordings are highly correlated with each other and with the ensemble average (black). These recordings were replotted in Fig. 4E by overlaying seven frames around every local maximum in the trajectory (guided with vertical dashed lines in Fig. 4D). The mean ΔF/F's over 23 cycles are plotted with thicker lines (black, ensemble ΔF/F; blue, red, green, and cyan, local ΔF/F's in Fig. 4A). This result demonstrates the fidelity of membrane potential recording with ANEPPPS.

The same analysis was performed for self-spiking HEK293 cells stained with pcNRs. In contrast to the clear membrane staining of ANEPPS (Fig. 4A), pcNRs are randomly distributed in the membrane and outside of it (cloudy background). In principle, better labeling (and higher contrast images) could be achieved by multiple washes applied to the tissue culture after incubation with pcNRs (as shown in Fig. 3E), but multiple washes abolish self-spiking. To eliminate densely pcNR-labeled regions and diffused background from the analysis of the data represented in Fig. 4B, a 10th-order ($n = 10$) Butterworth-type (high-pass) spatial filter (HPF_{pixel}) was applied to the image (fig. S7, A and B). The cutoff spatial frequency (ω_c) was 0.244 (pixel^{-1}). This image processing results in improved local contrast and enables the detection/identification of single bright spots (Fig. 4C). In a subsequent step, simple thresholding (threshold = mean + 2 $\cong$× SD) was applied to select

only bright, small pcNR-labeled regions (white pixels in fig. S8C) for calculating the ensemble ΔF/F. The spatially averaged (over all white pixels in fig. S8C) temporal fluorescence signal is shown in fig. S8D. Extracting the membrane potential fluctuation from this signal is difficult because of photo-brightening and noise.

Therefore, we implemented an additional temporal bandpass filtering step that is a 5th-order ($M = 5$) Butterworth filter with cutoff frequencies ($f_{high} = 7$ Hz and $f_{low} = 2.5$ Hz; fig. S8E). This process further cleans up and highlights these oscillations by removing the slowly varying (low-frequency) photo-brightening and the high frequency shot noise (Fig. 4F, top, black line). The filtered signal in Fig. 4F (top) exhibits ~4-Hz oscillations, similar to the oscillations reported in Fig. 4D. The asymmetric voltage depolarization and repolarization signal (49) is not resolved here because of the long integration time (30 ms). Although the ensemble ΔF/F is only ~1%, it demonstrates that pcNRs can record membrane voltage oscillation. To test whether pcNRs can provide single-particle voltage sensitivity, we analyzed isolated diffraction limited white spots in Fig. 4C (representing either individual pcNRs or very small aggregates of pcNRs). Bandpass-filtered optical recordings from the individual spots marked with colored open circles exhibit up to 5% ΔF/F voltage oscillations (Fig. 4F, cyan). Figure 4G shows (similar to Fig. 4E) signal time traces of 19 consecutive cycles (seven frames per cycle). The mean value of the signal is also shown with a thicker line. The same analysis was repeated for 129 individual diffraction-limited bright spots. Sixteen percent of all cases exhibited ΔF/F > 1%.

Additional evidence for voltage sensing by pcNRs was provided by simultaneous patch-clamp and fluorescence measurements. pcNRs were applied directly to wild-type HEK293 cells that were cultured on a coverslip, and fluorescence emission and membrane voltage were recorded simultaneously. Fluorescence movies were recorded in synchrony with the membrane voltage modulation (with a cycle of two movie frames recorded at −150 mV, followed by two movie frames recorded at 0 mV, voltage modulation frequency of 100 Hz, and recording duration of 2000 frames with 400 Hz of frame rate). Figure 5A shows a fluorescence time trajectory recorded from a single (or possibly a small aggregate of) pcNR(s) (as judged by blinking) highlighted by an arrow in Fig. 3F (a link to the movie is provided in section S9.1). The fluorescence trajectory is highly noisy, most likely due to fluorescence intermittency (blinking) and unstable, dynamic fluctuations in membrane insertion (see discussion about membrane insertion stability in section S9). A zoom-in to the trajectory at around 4.6 s (Fig. 5B) shows a zigzag pattern in the fluorescence intensity that is synchronized with the modulated clamped voltage. For each modulation semi-period, we defined a pcNR modulation response ΔF/F as the difference between voltage-on and voltage-off intensities divided by the mean time-trace intensity. The modulation response (ΔF/F) exhibits a high degree of variations throughout the acquisition time (5 s), with a few spikes of high signal about 100 ms long. We attribute the low reproducibility and low sensitivity of these recordings to the imperfect, unstable insertion of pcNRs into the cellular membrane.

We identified eight individual (or small cluster of) pcNRs in the patched cell's membrane (or its proximity), and for each, we computed the mean modulation response during the entire time trace (excluding the off periods due to the pcNR fluorescence blinking). Of eight pcNRs, only three exhibited a mean absolute modulation that was higher than the mean calculated for pcNRs in membranes of nonpatched cells.
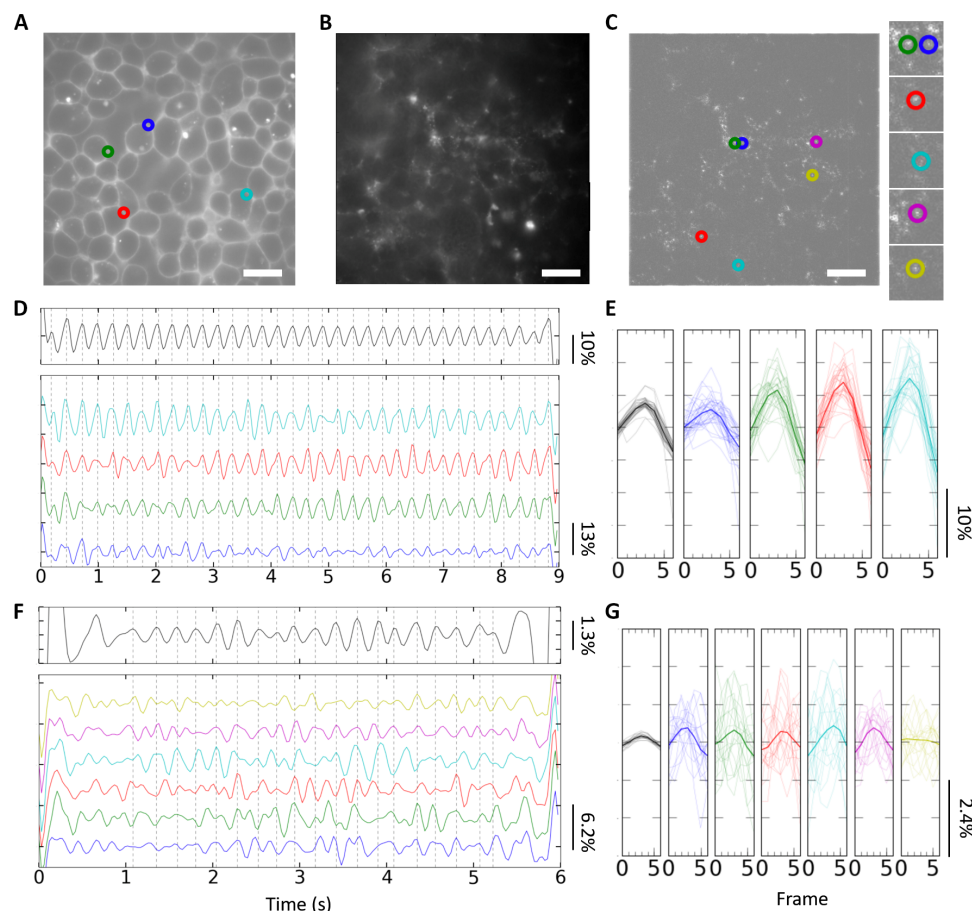
Fig. 4. Membrane voltage sensing of spiking HEK293 cells with pcNRs. (**A** and **B**) Fluorescence images of cells stained with ANEPPS (A) and pcNRs (B). (**C**) Spatially high-pass–filtered image of (B) used to highlight signals from individual pcNRs and remove background signals. (**D** and **F**) Temporal bandpass-filtered $\Delta F/F$ time trace of ANEPPS (D, top) and pcNRs (F, top). Each trace (D and F, bottom) shares the same color as the marked open circles in (A) or (C), respectively (see section S8). (**E** and **G**) Overlaid $\Delta F/F$'s of seven frames around the gray dashed lines in (D) and (F). (D) and (F) have 23 and 19 thin lines in each subplot, respectively. Mean traces are shown with thicker line width. The leftmost subplots with black lines are $\Delta F/F$ of ensemble average [generated from top in (D) and (F)]. Scale bars, 10 μm.

However, these three pcNRs all have a negative mean modulation (with a $\pm 1\sigma$ error range that does not include 0), whereas the control group of seven pcNRs in the membrane of nonpatched cells exhibits a mean signal, which is statistically indistinguishable from 0 (fig. S10). Because the modulation response $\Delta F/F$ exhibits spikes or "bursts" of high signal that presumably correspond to brief periods of membrane insertion, we carried out an objective analysis that is focused on these brief bursts. To reduce the effect of noise on the identification of the start and stop of burst regions, we thresholded the running average of the $\Delta F/F$ modulation response. We then computed the integral modulation response in each burst i as $S_i = \frac{1}{F}\sum_i \Delta F_i$ (see Materials and Methods and section S9 for the details on patch-clamp analysis). Figure 5C shows the distribution of integral modulation responses for bursts belonging to pcNRs found in the patched cell membrane (patched in-phase, red) compared to integral modulation responses of controls that should not exhibit any correlated signal. In particular, in the out-of-phase controls, we suppress any intensity fluctuation in-phase with the voltage modulation by averaging frames corresponding to on and off voltage semi-periods (see Materials and Methods). We observe that, although the controls exhibit a symmetric distribution of bursts with positive and negative values for the integral modulation response (consistent with

random fluctuations), bursts of patched pcNRs show a predominance of negative integral modulation response (consistent with fluorescence reduction induced by the applied voltage). However, note that only 18 in-phase bursts were identified and analyzed for the three pcNRs associated with the patched cell membrane (and 20 out-of-phase bursts). For the nonpatched cell control, we identified seven pcNRs (in non–nearest neighbor cells to avoid possible signal leakage) that yield a total of 28 in-phase bursts (and 40 out-of-phase bursts).

DISCUSSION

NRs have many advantages over organic fluorophores, having large voltage sensitivity, large absorption cross section, and reduced photobleaching. However, they are difficult to integrate into biological and neuroscience applications because of their large size and unknown surface properties that lead to nonspecific binding. Furthermore, inserting NRs into membrane bilayers presents additional challenges due to the need for sophisticated facet-selective surface functionalization for control of insertion orientation.

Here, we showed membrane insertion of pcNRs using α-helical peptides as the surface ligand of NRs, as demonstrated by TEM micrograph (Fig. 2A). On the basis of these observations and on a statistical
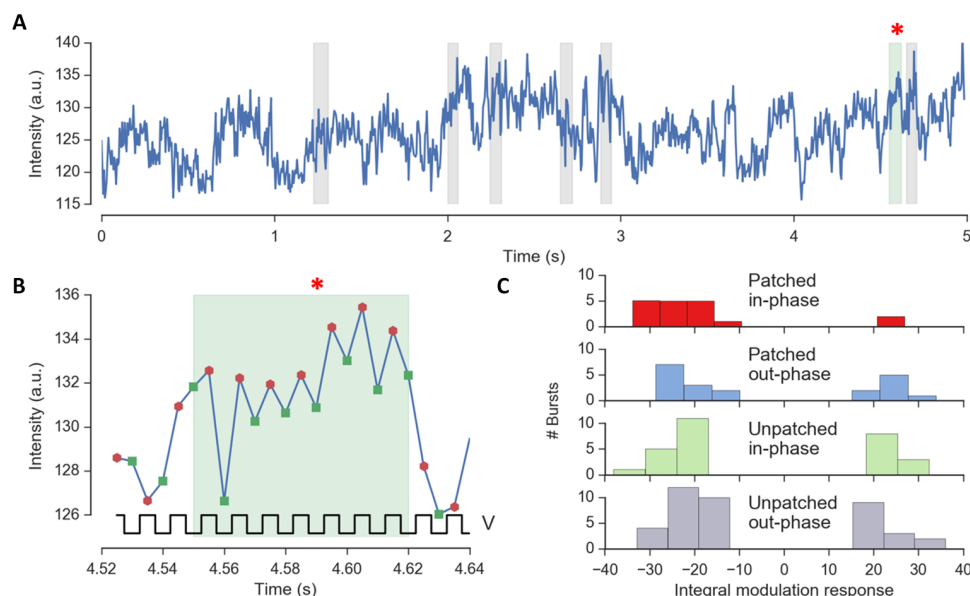
Fig. 5. Voltage response of pcNRs. (**A**) Intensity trace of a single pcNR with time intervals of large $\Delta F/F$ modulation response (bursts) marked with a shaded area and asterisk (*). (**B**) Zoom-in of intensity trace during a burst in (A); each marker represents a two-frame average intensity during the voltage-on (green squares) and voltage-off (red dots) semi-period. (**C**) Histogram of the modulation responses for each aggregating burst from many pcNRs in a video. The first group (red) represents the set of patched pcNRs that exhibit the highest signal. The other three distributions represent control groups for the set of unpatched pcNRs and/or for out-of-phase modulation response. a.u., arbitrary units.

mechanics–based theoretical investigation (Fig. 2E and section S7), we conclude that >60% of all membrane-associated pcNRs are favorably oriented (long axis parallel to the membrane's normal) but not necessarily fully inserted into the membrane. The polarization microscopy experiment also reveals that the subpopulation of NRs in GUVs is oriented in a favorable orientation (fig. S2). However, for highest voltage sensitivity, pcNRs need to be aligned as parallel to the membrane normal as possible (to guarantee maximal QCSE charge separation), with both tips exposed to the cytoplasm and extracellular matrix, respectively. The small fraction (~16% of all geometries) of NRs proves the proper insertion in the membrane, showing the feasibility of membrane potential sensing. Fluorescence signals could be recorded from individual membrane-inserted or membrane-associated pcNRs, as is evident from the typical temporal blinking (intermittency) pattern (50) in their emission (movie S1). The high brightness of pcNRs stems from their large absorption cross section and high-emission quantum yield (51). In the patch-clamp experiment, we used a scientific complementary metal-oxide semiconductor (sCMOS) camera and a 488-nm laser (see Material and Methods). With this optical system, we were able to run the camera at a 400-Hz frame rate (2.5-ms integration time per frame) while capturing the modulated signal. We estimate that if an electron-multiplying charge-coupled device (EMCCD) camera is used instead, then, together with a shorter-wavelength laser excitation (<450nm), the emission rate of the higher NR and the higher camera gain will result in a higher S/N ratio. Together, shorter-wavelength laser excitation and EM gain will yield higher S/N ratio, allowing for an acquisition rate of ~1 kHz but at the expense of working with a smaller region of interest through binning (because EMCCD camera acquisition rates are usually slower than those of sCMOS cameras). The absorption cross section of the NR could be further increased by adopting a lower bandgap material. Here, we used NRs consisting of CdSe (seed) and CdS (shell) with an optical bandgap of 600 nm. Using bandgap engineering and a different choice of materials' composition, the bandgap could be lowered toward the near-infrared, whereas excitation could be tuned to the blue/near-ultraviolet region

of the spectrum. In return, this will lead to an even higher single-NR brightness. We believe that by further improving the optical setup and the photon emission rate of the NR, it should be possible to record signals from individual NRs at >1-kHz rate and, hence, capture individual action potential spikes. Moreover, an increased photon emission rate will allow us to use advanced noise-immune voltage-sensing techniques such as lifetime imaging, spectrally separated ratiometric measurement, or a spectral shift measurement. These approaches are, to a large extent, immune to fluorescence intermittency. On the other hand, the simple intensity-based measurement reported here is highly sensitive to intermittency and therefore required filtering of the raw signals.

Overall, our results demonstrate that individual (or a small aggregate of) pcNR is capable of recording the membrane potential. The voltage sensitivity of an ensemble of membrane-inserted pcNRs in self-spiking HEK293 cells was quite poor (Fig. 4F), with a $\Delta F/F \sim 0.6\%$ (much lower than the sensitivity of ANEPPS, a typical voltage sensitive dye (VSD), exhibiting $\Delta F/F$ of ~10% in Fig. 4D). We attribute this poor performance to imperfect membrane insertion for a large fraction of the NRs. Although larger than 5% signal are captured in Fig. 4 (F and G) intermittently, the averaged $\Delta F/F$ of an individual NR is typically ~1%. This is likely due to the blinking feature of the NR and its dynamic movement/orientation fluctuation in the membrane. Because nonblinking nanocrystals are currently introduced, the photoluminescence (PL) fluctuation due to blinking will be improved (52). Because the study of the interaction energy between an NR and its environment (a solvent and a membrane) estimates the orientation of the NR quite accurately (Fig. 2, C to E), the optimized geometry for membrane insertion can be drawn with further theoretical investigation. To achieve stable and robust PL signal, more advanced surface functionalization should be pursued. To exploit the different surface energy between a cylinder wall and the tips of an NR, using face-selective surfactants (hydrophilic surfactants at the tips of the NR) will be one such example. Nonetheless, even with the current generation of NRs and coating, we could find a small fraction (~16%) of individual or small aggregate NRs exhibiting a sizeable $\Delta F/F \sim 5.0\%$.

In a second experiment, a voltage modulation of −150 to 0 mV (somewhat larger than a typical action potential of −70 to 40 mV) was applied to a patched (wild-type) HEK cell. Under this modulation, we were able to observe a higher in-phase modulation response of pcNRs that is statistically significant as compared to unpatched cells, whereas the control experiment (out-of-phase analysis) shows no modulation response, as expected (Fig. 5C). The sensitivity, the noise level, and the temporal resolution of these measurements are as of yet inadequate for electrophysiological recording.

The data presented in Figs. 4 and 5 suggest that with further improvements, pcNRs could be suitable for membrane potential recording. Marshall and Schnitzer (35) estimated 5 and 30% of $\Delta F/F$ during neuronal spiking with type I and type II QDs, respectively. The signal quality could be greatly increased by a series of enhancements. For example, preliminary experiments and calculations suggest that seeded NR heterostructures with type II band offset and large seed position asymmetry could exhibit very high voltage sensitivity (34). Moreover, improved membrane insertion stability will reduce measurement noise and enhance the signal. Last, as previously shown (34), shifts in the spectral peak position are considerably more sensitive than $\Delta F/F$ changes. A simple modification to the optical setup (based on "dual-view" microscopy) (53) could enhance voltage sensitivity even further.

Development of high-sensitivity pcNRs could afford unprecedented ways to study electrical activities in neuronal, neuromuscular, and visual systems on the nanoscale (such as across a single synapse) or the ability to record a large number of signals from a large field of view (high-throughput recording). pcNRs could also find applications in other areas of science and engineering, for example, in inducing action potential (54, 55), characterization of high-density fast integrated circuits, and energy harvesting by membrane-inserted artificial light-harvesting complexes. Last, the ability to impart membrane protein–like properties to inorganic and organic NPs could allow the construction of novel membrane-based hybrid (organic-inorganic) materials with unique exploitable properties.

MATERIALS AND METHODS
Quasi type II NRs synthesis (CdSe seeded in CdS)
Cadmium oxide (CdO; 99.99%), tri-*n*-octylphosphine (TOP; 90%), trioctylphosphine oxide (TOPO; 99%), selenium (Se; 99.999%), and sulfur (S; 99.5%) along with all organic solvents were purchased from Sigma-Aldrich and used without any further purification. Hexylphosphonic acid (HPA) and octadecylphosphonic (ODPA) were purchased from PCI Synthesis. A 50-ml round-bottom flask was loaded with 60 mg (0.5 mmol) of CdO, 280 mg of ODPA, and 3 g of TOPO. After degassing under a vacuum for 1 hour at 120°C, the temperature was raised to 340°C under argon until dissolution of CdO at which point 1.8 ml of TOP was injected and temperature was raised to 370°C. A solution containing 58 mg of Se in 0.5 ml of TOP was swiftly injected, and the heating mantle was removed. The final core size had a diameter of about 2.7 nm. A slight modification of previously reported methods (7) was used for seeded growth of CdS. A 50-ml round-bottom flask was charged with 211 mg (1.6 mmol) of CdO, 1 g of ODPA, 50 mg of HPA, and 3.46 g of TOPO. The reaction flask was degassed for 3 hours at 130°C, and then, temperature was raised to 340°C under argon until dissolution of CdO at which point 1.8 ml of TOP was injected. The CdSe seed solution was separated and purified for reaction by mixing three times with toluene and precipitating with excess methanol. Seeds were then redissolved in 0.6 ml of

TOP. The S:TOP precursor solution was prepared by mixing 51 mg of S (1.6 mmol) in 0.6 ml of TOP. Temperature was raised to 350°C for injection. The amount of dots used was 8×10^{-7} mol. The size distribution of NRs was characterized by EM, yielding 4 ± 0.3 and 10 ± 2.2 nm for the diameter and length of NRs, respectively.

NR functionalization with peptides
The sequence of the two peptides used in this study was myristoyl-CLTCALTCMECTLKCWYKRGCRCG-COOH. Peptides were purchased from LifeTein LLC, purified to a level of 70% by high-performance liquid chromatography, characterized by mass spectrometry and circular dichroism (fig. S1). The protocol for NR functionalization with α-helical peptides was similar to that reported by Pinaud *et al.* (39), with the following modifications: As-synthesized NRs were coated with hydrophobic surfactants such as TOPO or ODPA. To exchange these surfactants with the designed peptides, we first stripped the surfactants off the NRs by multiple (five to six times) methanol precipitation steps, followed by redissolution in 450 μl of pyridine. The concentration of the NR was 0.1 μM. Four milligrams of peptides was dissolved in 50 μl of dimethyl sulfoxide (DMSO) and mixed with NRs in DMSO solution. Twelve microliters of tetramethylammonium hydroxide was added to the solution to increase the pH to 10.0, allowing the peptides to bind to the surface of NRs efficiently. The mixture was then centrifuged and redispersed in 150 μl of DMSO in a form ready to be used for cell membrane insertion (staining). For vesicle staining or for cryoEM experiment, NRs in DMSO solution were eluted through a Sephadex G-25 desalting column (Amersham) and equilibrated with phosphate-buffered saline (PBS) buffer. The pcNRs were stored at 4°C. As-synthesized NRs emitted photons of 600 nm. Their initial quantum yield was 15%, which was maintained after the peptide-coating process.

Loading pcNRs into vesicles
1,2-Dimyristoyl-*sn*-glycero-3-phosphocholine (DMPC), DOTAP, and DC-Chol were purchased from Avanti Polar Lipids Inc. Chloroform solutions of DOTAP (25 mM, 6 μl), DMPC (10 mM, 6 μl), and DC-Chol (10 mM, 6 μl) were mixed and dried in a vacuum for 4 hours in a rotary evaporator. The film was then hydrated with 1 ml of 0.1 M sucrose containing PBS buffer (pH 6.24) overnight at 37°C incubator, during which vesicles were spontaneously formed. Vesicles were stored at 4°C, unless used in experiments (they are stable and useable for about 1 week). For the cryoEM experiment, vesicles were extruded through a membrane with 100-nm pore-sized filter. For fluorescence microscopy measurement, 2 μl of pcNRs (eluted through a Sephadex G-25 desalting column) was added to the 10 μl of vesicle solution. pcNRs spontaneously and rapidly (~1 min) self-inserted into the vesicles' membranes. For GUVs, the same lipid composition (6 μl of 25 mM DOTAP, 6 μl of 10 mM DMPC, and 6 μl of 10 mM DC-Chol) was diluted with 200 μl of chloroform. Fifty microliters of the lipid in chloroform solution was loaded on the indium tin oxide (ITO)–coated glass. After 30 min of drying, the other ITO-coated glass was faced to the lipid-dried ITO glass. Two glasses are separated by the 3-mm thickness of O-ring, forming the aqueous chamber for electro-swelling. A square-voltage pulse (10 Hz of 1.0 V) was applied to the two ITO glasses for 20 min, followed by GUV preparation for imaging.

CryoEM
For the cryoEM measurement, 10 μl of pcNRs (eluted through a Sephadex G-25 desalting column, producing 0.05 μM) was added to 50 μl of vesicle solution (lipid concentration, 0.27 mM). An aliquot

(3 µl) of sample was placed on holey carbon-coated Quantifoil grid, manually blotted with filter paper, and plunged into liquid ethane to make an cryoEM grid with vesicles embedded in vitreous ice. The grid was transferred to a Gatan 626 cryo-sample holder cooled down by liquid nitrogen and inserted into an FEI TF20 cryo-electron microscope for imaging at 200-kV operating voltage. Images were recorded at several magnifications on a 4k × 4k CCD camera (Tietz Video and Image Processing Systems) at ~5 µm under focus, with an accumulated electron dosage of ~20 e⁻/Å² on each sample area.

Cell culture and staining

HEK293 cells (American Type Culture Collection) were maintained in 1:1 Dulbecco's modified Eagle medium and nutrient mixture F-12 (Invitrogen) supplemented with 10% fetal bovine serum (Sigma-Aldrich), geneticin (0.6 mg/ml; G418, Life Technologies), and puromycin (5 µg/ml; Life Technologies). Cells were grown on 35-mm glass-bottom dishes until they reached 90% confluency. The same protocol was applied to self-spiking HEK293 cells. For ANEPPS staining, ANEPPS solution in DMSO was added directly to the cells in a 35-mm glass-bottom dish to a final concentration of 0.1 µM. Cells were then incubated at 4°C for 5 min before imaging.

Optical imaging and data acquisition of the fluorescence signal of pcNRs in self-spiking HEK293 cells

The microscope setup was based on an Olympus IX71 inverted microscope equipped with a xenon lamp (75 W; U-LH75XEAPO, Olympus) and excitation filter (BP 470/40, Chroma Technology Corp). The excitation power was 2 mW at the image plane. The emission of the NPs was collected by a 60× objective lens (PlanApo 60×, NA = 1.45, oil immersion, Olympus) and passed through a dichroic mirror (505DCXRU, Chroma Technology Corp). Imaging was carried out with an Andor iXon EMCCD camera (Andor iXon). Two microliters of pcNRs in DMSO solution (~300 nM) were loaded to the glass-bottom dish (Thermo Fisher Scientific) where the self-spiking HEK293 cells were cultured. The pcNRs spontaneously inserted into cell membranes within 1 to 2 min. The pcNR-loading density estimated from the image was ~10⁵ pcNRs per cell. After rapid shaking, the cell medium was changed with Dulbecco's PBS (Life Technologies). The dish was then placed on the microscope. Fluorescence was recorded in a movie format for 9 s with a 30-ms integration per frame.

Simultaneous patch-clamp recording and fluorescence imaging

Two microliters of pcNRs were added directly to the cell culture (in a 35-mm glass-bottom dish with 2 ml of cell culture medium). Cells were then incubated at 37°C for 5 min before patch-clamp recording and imaging. As estimated from images, an average of ~10 particles were inserted into each cell. The loading density is approximated to be ~10⁻⁷ pcNRs/nm². All imaging and electrophysiology were performed in Tyrode's buffer (pH 7.3; containing 125 mM NaCl, 2.5 mM KCl, 3 mM CaCl₂, 1 mM MgCl₂, 10 mM Hepes, and 30 mM glucose and adjusted to 305 to 310 mosmol with sucrose). For patch clamp, filamented glass micropipettes (WPI) were pulled to a tip resistance of 5 to 10 megohm and filled with internal solution containing 125 mM potassium gluconate, 8 mM NaCl, 0.6 mM MgCl₂, 0.1 mM CaCl₂, 1 mM EGTA, 10 mM Hepes, 4 mM Mg–ATP (adenosine 5′-triphosphate), and 0.4 mM Na–GTP (guanosine 5′-triphosphate) (pH 7.3) and adjusted to 295 mosmol with sucrose. Pipettes were positioned with a Sutter MP-285 manipulator. Whole-cell, voltage, and current-clamp

recordings were acquired using a patch-clamp amplifier (model 2400, A-M Systems), filtered at 5 kHz with the internal filter, and digitized with a National Instruments PCIe-6323 acquisition board at 10 kHz. Simultaneous whole-cell patch-clamp recordings and fluorescence recordings were acquired on a home-built, inverted epifluorescence microscope equipped with a 60× water immersion objective, numerical aperture 1.20 (Olympus UIS2 UPlanSApo 60×/1.20 W), a long-pass dichroic filter (Chroma zt505-515+650NIR Tpc), and a scientific CMOS camera (Hamamatsu ORCA Flash 4.0). Laser intensity (488 nm; Coherent Obis 488-50) was modulated with an acousto-optic tunable filter (Gooch and Housego 48058-2.5-.55-5W). Imaging of pcNRs was performed at illumination intensities of ~1 W cm⁻². For fast data acquisition, a small field of view around the cell of interest was chosen at the center of the camera to achieve a frame rate of 1000 frames/s.

Data analysis of pcNRs' fluorescence during patch-clamp recording

From the video, we manually identified the position of pcNRs on both the patched cell membrane and on nonpatched cells. For each identified pcNRs, the time trace of emission intensity $\{t_k\}$ was obtained by averaging, for each frame k, a circular region of approximately 20 pixels around the pcNR. The time-trace intensity was binned to each of two frames to obtain an intensity $\{\bar{t}_j\}$ for each voltage alternation semi-period, and then, the difference $\{\Delta F_i\}$ was computed as $\{(\bar{t}_1 - \bar{t}_0), -(\bar{t}_2 - \bar{t}_1), (\bar{t}_3 - \bar{t}_2), -(\bar{t}_4 - \bar{t}_3), ...\}$ (the signal alternates and is "+" and "−" for on-off and off-on transitions, respectively). Finally, these differences were divided by the average time-trace intensity to obtain the signal $\{\Delta F_i/F\}$.

The burst search was performed as follows. The square of the running average of the modulation response $\{\Delta F_i/F\}$ was computed, and the time periods where this squared average was higher than a threshold (set to 60% of the maximum) were identified as bursts. Next, for each burst i, we extracted the total signal (burst score) $S_i = \frac{1}{F}\sum_i \Delta F_i$. The out-of-phase response was obtained by removing the first video frame and applying the same analysis on the time traces. In this case, the binning step averaged frames between on and off semi-periods, suppressing any signal in-phase with the voltage alternation. See section S9 for detailed description of the patch-clamp data analysis.

SUPPLEMENTARY MATERIALS

Supplementary material for this article is available at http://advances.sciencemag.org/cgi/content/full/4/1/e1601453/DC1

section S1. Design of the peptide sequence for coating NRs
section S2. Circular dichroism of the designed peptide
section S3. Fluorescence anisotropy of pcNR-loaded vesicles
section S4. Cell membrane staining with pcNRs
section S5. CryoEM control: Ligand-coated NRs do not insert into vesicles' membranes
section S6. Endocytosis of pcNRs after 1 hour of loading
section S7. Simulation of the energetics of the NR in the membrane
section S8. Optical recording of ANEPPS-labeled and pcNR-labeled spiking HEK cells
section S9. Simultaneous optical and electrical recordings in patch-clamp experiment
fig. S1. Circular dichroism spectrum of designed peptides dissolved in octanol.
fig. S2. Orientation-dependent AA of pcNRs in membranes of GV.
fig. S3. Confocal cross-sections of an HEK293 cell fused with pcNR-loaded vesicles.
fig. S4. CryoEM images of vesicles after incubation with pcNRs.
fig. S5. Images of pcNR-loaded HEK293 cells taken 1 hour later.
fig. S6. Canting angle distribution of NR.
fig. S7. Image processing of voltage recording with ANEPPS.
fig. S8. Image processing of voltage recording with pcNR.

fig. S9. Mean of $\{\Delta F_i/F\}$ for the two sets of patched (left) and unpatched (right) particles.
fig. S10. Image processing of voltage recording with pcNRs.
table S1. Absorption anisotropy of NRs in the membrane.
movie S1. Fluorescence movie of pcNR-stained HEK293 cells.
Reference (56)

REFERENCES AND NOTES

1. C. B. Murray, D. J. Norris, M. G. Bawendi, Synthesis and characterization of nearly monodisperse CdE (E = sulfur, selenium, tellurium) semiconductor nanocrystallites. *J. Am. Chem. Soc.* **115**, 8706–8715 (1993).

2. X. Peng, L. Manna, W. Yang, J. Wickham, E. Scher, A. Kadavanich, A. P. Alivisatos, Shape control of CdSe nanocrystals. *Nature* **404**, 59–61 (2000).

3. Z. A. Peng, X. Peng, Nearly monodisperse and shape-controlled CdSe nanocrystals via alternative routes: Nucleation and growth. *J. Am. Chem. Soc.* **124**, 3343–3353 (2002).

4. L. Manna, E. C. Scher, A. P. Alivisatos, Synthesis of soluble and processable rod-, arrow-, teardrop-, and tetrapod-shaped CdSe nanocrystals. *J. Am. Chem. Soc.* **122**, 12700–12706 (2000).

5. D. V. Talapin, J. H. Nelson, E. V. Shevchenko, S. Aloni, B. Sadtler, A. P. Alivisatos, Seeded growth of highly luminescent CdSe/CdS nanoheterostructures with rod and tetrapod morphologies. *Nano Lett.* **7**, 2951–2959 (2007).

6. J. Müller, J. M. Lupton, P. G. Lagoudakis, F. Schindler, R. Koeppe, A. L. Rogach, J. Feldmann, D. V. Talapin, H. Weller, Wave function engineering in elongated semiconductor nanocrystals with heterogeneous carrier confinement. *Nano Lett.* **5**, 2044–2049 (2005).

7. N. N. Hewa-Kasakarage, M. Kirsanova, A. Nemchinov, N. Schmall, P. Z. El-Khoury, A. N. Tarnovsky, M. Zamkov, Radiative recombination of spatially extended excitons in (ZnSe/CdS)/CdS heterostructured nanorods. *J. Am. Chem. Soc.* **131**, 1328–1334 (2009).

8. J. Müller, J. M. Lupton, A. L. Rogach, J. Feldmann, D. V. Talapin, H. Weller, Monitoring surface charge migration in the spectral dynamics of single CdSe/CdS nanodot/nanorod heterostructures. *Phys. Rev. B* **72**, 205339 (2005).

9. T.-H. Kim, K.-S. Cho, E. K. Lee, S. J. Lee, J. Chae, J. W. Kim, D. H. Kim, J.-Y. Kwon, G. Amaratunga, S. Y. Lee, B. L. Choi, Y. Kuk, J. M. Kim, K. Kim, Full-colour quantum dot displays fabricated by transfer printing. *Nat. Photonics* **5**, 176–182 (2011).

10. V. I. Klimov, S. A. Ivanov, J. Nanda, M. Achermann, I. Bezel, J. A. McGuire, A. Piryatinski, Single-exciton optical gain in semiconductor nanocrystals. *Nature* **447**, 441–446 (2007).

11. X. Michalet, F. F. Pinaud, L. A. Bentolila, J. M. Tsay, S. Doose, J. J. Li, G. Sundaresan, A. M. Wu, S. S. Gambhir, S. Weiss, Quantum dots for live cells, in vivo imaging, and diagnostics. *Science* **307**, 538–544 (2005).

12. S. Li, K. Zhang, J.-M. Yang, L. Lin, H. Yang, Single quantum dots as local temperature markers. *Nano Lett.* **7**, 3102–3105 (2007).

13. M. J. Ruedas-Rama, E. A. H. Hall, Azamacrocycle activated quantum dot for zinc ion detection. *Anal. Chem.* **80**, 8260–8268 (2008).

14. H. Aouani, S. Itzhakov, D. Gachet, E. Devaux, T. W. Ebbesen, H. Rigneault, D. Oron, J. Wenger, Colloidal quantum dots as probes of excitation field enhancement in photonic antennas. *ACS Nano* **4**, 4571–4578 (2010).

15. H. Zhu, N. Song, H. Lv, C. L. Hill, T. Lian, Near unity quantum yield of light-driven redox mediator reduction and efficient H$_2$ generation using colloidal nanorod heterostructures. *J. Am. Chem. Soc.* **134**, 11701–11708 (2012).

16. I. N. Mora-Seró, J. Bisquert, Breakthroughs in the development of semiconductor-sensitized solar cells. *J. Phys. Chem. Lett.* **1**, 3046–3052 (2010).

17. J. B. Delehanty, I. L. Medintz, T. Pons, F. M. Brunel, P. E. Dawson, H. Mattoussi, Self-assembled quantum dot–peptide bioconjugates for selective intracellular delivery. *Bioconjugate Chem.* **17**, 920–927 (2006).

18. P. Pandey, S. P. Singh, S. K. Arya, V. Gupta, M. Datta, S. Singh, B. D. Malhotra, Application of thiolated gold nanoparticles for the enhancement of glucose oxidase activity. *Langmuir* **23**, 3333–3337 (2007).

19. G. Tikhomirov, S. Hoogland, P. E. Lee, A. Fischer, E. H. Sargent, S. O. Kelley, DNA-based programming of quantum dot valency, self-assembly and luminescence. *Nat. Nanotechnol.* **6**, 485–490 (2011).

20. I. L. Medintz, H. T. Uyeda, E. R. Goldman, H. Mattoussi, Quantum dot bioconjugates for imaging, labelling and sensing. *Nat. Mater.* **4**, 435–446 (2005).

21. I. L. Medintz, M. H. Stewart, S. A. Trammell, K. Susumu, J. B. Delehanty, B. C. Mei, J. S. Melinger, J. B. Blanco-Canosa, P. E. Dawson, H. Mattoussi, Quantum-dot/dopamine bioconjugates function as redox coupled assemblies for in vitro and intracellular pH sensing. *Nat. Mater.* **9**, 676–684 (2010).

22. J. Xu, J. Teslaa, T.-H. Wu, P.-Y. Chiou, M. A. Teitell, S. Weiss, Nanoblade delivery and incorporation of quantum dot conjugates into tubulin networks in live cells. *Nano Lett.* **12**, 5669–5672 (2012).

23. M. L. Schipper, G. Iyer, A. L. Koh, Z. Cheng, Y. Ebenstein, A. Aharoni, S. Keren, L. A. Bentolila, J. Q. Li, J. Rao, X. Chen, U. Banin, A. M. Wu, R. Sinclair, S. Weiss, S. S. Gambhir, Particle size, surface coating, and PEGylation influence the biodistribution of quantum dots in living mice. *Small* **5**, 126–134 (2009).

24. J. B. Blanco-Canosa, M. Wu, K. Susumu, E. Petryayeva, T. L. Jennings, P. E. Dawson, W. R. Algar, I. L. Medintz, Recent progress in the bioconjugation of quantum dots. *Coord. Chem. Rev.* **263–264**, 101–137 (2014).

25. W. T. Al-Jamal, K. T. Al-Jamal, B. Tian, L. Lacerda, P. H. Bomans, P. M. Frederik, K. Kostarelos, Lipid–quantum dot bilayer vesicles enhance tumor cell uptake and retention in vitro and in vivo. *ACS Nano* **2**, 408–418 (2008).

26. J. A. Kloepfer, N. Cohen, J. L. Nadeau, FRET between CdSe quantum dots in lipid vesicles and water- and lipid-soluble dyes. *J. Phys. Chem. B* **108**, 17042–17049 (2004).

27. G. Gopalakrishnan, C. Danelon, P. Izewska, M. Prummer, P.-Y. Bolinger, I. Geissbühler, D. Demurtas, J. Dubochet, H. Vogel, Multifunctional lipid/quantum dot hybrid nanocontainers for controlled targeting of live cells. *Angew. Chem. Int. Ed.* **45**, 5478–5483 (2006).

28. H. S. Wi, S. J. Kim, K. Lee, S. M. Kim, H. S. Yang, H. K. Pak, Incorporation of quantum dots into the lipid bilayer of giant unilamellar vesicles and its stability. *Colloids Surf. B Biointerfaces* **97**, 37–42 (2012).

29. M. Langecker, V. Arnaut, T. G. Martin, J. List, S. Renner, M. Mayer, H. Dietz, F. C. Simmel, Synthetic lipid membrane channels formed by designed DNA nanostructures. *Science* **338**, 932–936 (2012).

30. A. Seifert, K. Göpfrich, J. R. Burns, N. Fertig, U. F. Keyser, S. Howorka, Bilayer-spanning DNA nanopores with voltage-switching between open and closed state. *ACS Nano* **9**, 1117–1126 (2015).

31. J. Geng, K. Kim, J. Zhang, A. Escalada, R. Tunuguntla, L. R. Comolli, F. I. Allen, A. V. Shnyrova, K. R. Cho, D. Munoz, Y. M. Wang, C. P. Grigoropoulos, C. M. Ajo-Franklin, V. A. Frolov, A. Noy, Stochastic transport through carbon nanotubes in lipid bilayers and live cell membranes. *Nature* **514**, 612–615 (2014).

32. K. Becker, J. M. Lupton, J. Müller, A. L. Rogach, D. V. Talapin, H. Weller, J. Feldmann, Electrical control of Förster energy transfer. *Nat. Mater.* **5**, 777–781 (2006).

33. R. M. Kraus, P. G. Lagoudakis, A. L. Rogach, D. V. Talapin, H. Weller, J. M. Lupton, J. Feldmann, Room-temperature exciton storage in elongated semiconductor nanocrystals. *Phys. Rev. Lett.* **98**, 017401 (2007).

34. K. Park, Z. Deutsch, J. J. Li, D. Oron, S. Weiss, Single molecule quantum-confined Stark effect measurements of semiconductor nanoparticles at room temperature. *ACS Nano* **6**, 10013–10023 (2012).

35. J. D. Marshall, M. J. Schnitzer, Optical strategies for sensing neuronal voltage using quantum dots and other semiconductor nanocrystals. *ACS Nano* **7**, 4601–4609 (2013).

36. J. M. Kralj, A. D. Douglass, D. R. Hochbaum, D. Maclaurin, A. E. Cohen, Optical recording of action potentials in mammalian neurons using a microbial rhodopsin. *Nat. Methods* **9**, 90–95 (2012).

37. E. W. Miller, J. Y. Lin, E. P. Frady, P. A. Steinbach, W. B. Kristan Jr., R. Y. Tsien, Optically monitoring voltage in neurons by photo-induced electron transfer through molecular wires. *Proc. Natl. Acad. Sci. U.S.A.* **109**, 2114–2119 (2012).

38. K. Park, S. Weiss, Design rules for membrane-embedded voltage-sensing nanoparticles. *Biophys. J.* **112**, 703–713 (2017).

39. F. Pinaud, D. King, H.-P. Moore, S. Weiss, Bioactivation and cell targeting of semiconductor CdSe/ZnS nanocrystals with phytochelatin-related peptides. *J. Am. Chem. Soc.* **126**, 6115–6123 (2004).

40. F. Pinaud, X. Michalet, L. A. Bentolila, J. M. Tsay, S. Doose, J. J. Li, G. Iyer, S. Weiss, Advances in fluorescence imaging with quantum dot bio-probes. *Biomaterials* **27**, 1679–1687 (2006).

41. J. M. Tsay, S. Doose, F. Pinaud, S. Weiss, Enhancing the photoluminescence of peptide-coated nanocrystals with shell composition and UV irradiation. *J. Phys. Chem. B* **109**, 1669–1674 (2005).

42. G. Iyer, F. Pinaud, J. Tsay, S. Weiss, Solubilization of quantum dots with a recombinant peptide from *Escherichia coli*. *Small* **3**, 793–798 (2007).

43. G. Iyer, X. Michalet, Y.-P. Chang, F. F. Pinaud, S. E. Matyas, G. Payne, S. Weiss, High affinity scFv–hapten pair as a tool for quantum dot labeling and tracking of single proteins in live cells. *Nano Lett.* **8**, 4618–4623 (2008).

44. A. Senes, D. C. Chadi, P. B. Law, R. F. S. Walters, V. Nanda, W. F. DeGrado, E_z, a depth-dependent potential for assessing the energies of insertion of amino acid side-chains into membranes: Derivation and applications to determining the orientation of transmembrane and interfacial helices. *J. Mol. Biol.* **366**, 436–448 (2007).

45. I. Wrobel, D. Collins, Fusion of cationic liposomes with mammalian cells occurs after endocytosis. *Biochim. Biophys. Acta* **1235**, 296–304 (1995).

46. D. Axelrod, Carbocyanine dye orientation in red cell membrane studied by microscopic fluorescence polarization. *Biophys. J.* **26**, 557–574 (1979).

47. J. Xu, P. Ruchala, Y. Ebenstein, J. J. Li, S. Weiss, Stable, compact, bright biofunctional quantum dots with improved peptide coating. *J. Phys. Chem. B* **116**, 11370–11378 (2012).

48. C. Lonez, M. F. Lensink, E. Kleiren, J.-M. Vanderwinden, J.-M. Ruysschaert, M. Vandenbranden, Fusogenic activity of cationic lipids and lipid shape distribution. *Cell. Mol. Life Sci.* **67**, 483–494 (2010).

49. J. Park, C. A. Werley, V. Venkatachalam, J. M. Kralj, S. D. Dib-Hajj, S. G. Waxman, A. E. Cohen, Screening fluorescent voltage indicators with spontaneously spiking HEK cells. *PLOS ONE* **8**, e85221 (2013).

50. M. Nirmal, B. O. Dabbousi, M. G. Bawendi, J. J. Macklin, J. K. Trautman, T. D. Harris, L. E. Brus, Fluorescence intermittency in single cadmium selenide nanocrystals. *Nature* **383**, 802–804 (1996).

51. D. V. Talapin, R. Koeppe, S. Götzinger, A. Kornowski, J. M. Lupton, A. L. Rogach, O. Benson, J. Feldmann, H. Weller, Highly emissive colloidal CdSe/CdS heterostructures of mixed dimensionality. *Nano Lett.* **3**, 1677–1681 (2003).

52. J. I. Climente, J. L. Movilla, J. Planelles, Auger recombination suppression in nanocrystals with asymmetric electron–hole confinement. *Small* **8**, 754–759 (2012).

53. K. Kinosita, H. Itoh, S. Ishiwata, K. Hirano, T. Nishizaka, T. Hayakawa, Dual-view microscopy with a single camera: Real-time imaging of molecular orientations and calcium. *J. Cell Biol.* **115**, 67–73 (1991).

54. E. Molokanova, J. A. Bartel, W. Zhao, I. Naasani, M. J. Ignatius, J. A. Treadway, A. Savtchenko, Quantum dots move beyond fluorescence imaging. *Biophotonics Int.* 26–31 (2008).

55. E. Molokanova, A. Savchenko, Bright future of optical assays for ion channel drug discovery. *Drug Discov. Today* **13**, 14–22 (2008).

56. H. Shen, Interactive notebooks: Sharing the code. *Nature* **515**, 151–152 (2014).

Citation: K. Park, Y. Kuo, V. Shvadchak, A. Ingargiola, X. Dai, L. Hsiung, W. Kim, H. Zhou, P. Zou, A. J. Levine, J. Li, S. Weiss, Membrane insertion of—and membrane potential sensing by—semiconductor voltage nanosensors: Feasibility demonstration. *Sci. Adv.* **4**, e1601453 (2018).

Science Advances

Membrane insertion of—and membrane potential sensing by—semiconductor voltage nanosensors: Feasibility demonstration

Kyoungwon Park, Yung Kuo, Volodymyr Shvadchak, Antonino Ingargiola, Xinghong Dai, Lawrence Hsiung, Wookyeom Kim, Hong Zhou, Peng Zou, Alex J. Levine, Jack Li and Shimon Weiss

ARTICLE TOOLS	http://advances.sciencemag.org/content/4/1/e1601453
SUPPLEMENTARY MATERIALS	http://advances.sciencemag.org/content/suppl/2018/01/08/4.1.e1601453.DC1
REFERENCES	This article cites 55 articles, 4 of which you can access for free http://advances.sciencemag.org/content/4/1/e1601453#BIBL
PERMISSIONS	http://www.sciencemag.org/help/reprints-and-permissions

Use of this article is subject to the Terms of Service